Composites Part A 124 (2019) 105460

Contents lists available at ScienceDirect

Composites Part A

journal homepage: www.elsevier.com/locate/compositesa

Multi-scale modeling of mechanical behavior of cured woven textile composites accounting for the influence of yarn angle variation

Biao Liang[a], Weizhao Zhang[a], Joel S. Fenner[a], Jiaying Gao[a], Yi Shi[a], Danielle Zeng[b], Xuming Su[b], Wing K. Liu[a], Jian Cao[a,*]

[a] Department of Mechanical Engineering, Northwestern University, Evanston, IL 60208, United States
[b] Research & Advanced Engineering, Ford Motor Company, Dearborn, MI 48121, United States

ARTICLE INFO

Keywords:
Woven composites
Multi-scale modeling
Yarn angle
Material properties

ABSTRACT

In most current works related to the structure analysis of cured woven composites, the influence of yarn angle variation on the local material properties is neglected. In this paper, its influence was studied, and an integrated preforming-performance simulation model, accounting for the influence of yarn angle variation, was proposed. The multi-scale modeling approach was adopted to predict the material properties of cured woven composites with different yarn angles. The results were compared with experiments to validate its effectiveness. In the integrated preforming-performance simulation model, non-orthogonal constitutive law was used in the preforming simulation to compute yarn orientations and yarn angle distribution. To demonstrate the capabilities of the integrated simulation model, simulations were conducted and compared with experiments. The results show that the proposed simulation model has more accurate prediction than the simulation model without considering the influence of yarn angle, and the impact of yarn angle shouldn't be neglected.

1. Introduction

It is estimated that 75% of vehicle fuel consumption directly relates to its weight [1]. To address this issue, in recent years, automakers utilize more and more composites for their vehicles to reduce mass and to improve fuel efficiency [2]. Woven textile composites draw considerable attention due to their superior mechanical properties and favorable drapability of their reinforcements. They are increasingly utilized in the auto industry to manufacture composite parts and structures, such as bumpers, floor panels and body frames [1].

Woven textile composites can be described at least in three different length scales based on their constituents: micro, meso and macro (Fig. 1). Micro-scale refers to the scale of fiber and explicitly defines fiber distribution in the yarn. Yarn is the basic element at the meso-scale, which is composed of fiber and matrix, and characterizes the weaving pattern of woven textile composites. Macro-scale generally refers to the structure scale, and at this scale woven textile composites are usually treated as equivalent continuous materials. The multi-scale nature of woven textile composites leads to their material properties not only depending on their constituents, but also on their mesostructure.

At the meso-scale, Bednarcyk et al. [3] investigated the influence of the yarn aspect ratio (the width of yarn cross-section to its height) on the macro-material properties of cured woven composites. They found that variation of the yarn aspect ratio caused approximately three times more variation for the macro-tensile properties compared to the macro-shear properties. Similar work was performed by Green et al. [4]. They built two cured woven RVE structures: one used the idealized yarn geometry, and the other used the realistic yarn geometry measured from the computed tomography (CT) scan. The predicted macro-material properties from the realistic yarn geometry showed a better agreement with the experiment than the idealized yarn RVE model, indicating the importance of capturing yarn geometry accurately in meso-scale modeling and homogenization.

Nevertheless, in previously published works related to 2D woven textile composites homogenization [5–8], yarn angle, which is the angle between the weft- and warp -yarn directions as shown in Fig. 2(a), has always been assumed as 90° for the 2D woven RVE structure, and the homogenized material properties were used to characterize the material properties of the cured woven composite part. Local material property changes caused by the yarn angle variation have not been considered. For instance, in the work of Liu et al. [6] and Ning et al. [7], the homogenized material properties of the orthogonal woven RVE structure (yarn angle 90°) were directly applied in the crash and performance simulation of the cured woven composite part. They assumed

* Corresponding author.
E-mail address: jcao@northwestern.edu (J. Cao).

https://doi.org/10.1016/j.compositesa.2019.05.028
Received 16 November 2018; Received in revised form 17 April 2019; Accepted 21 May 2019
Available online 22 May 2019
1359-835X/

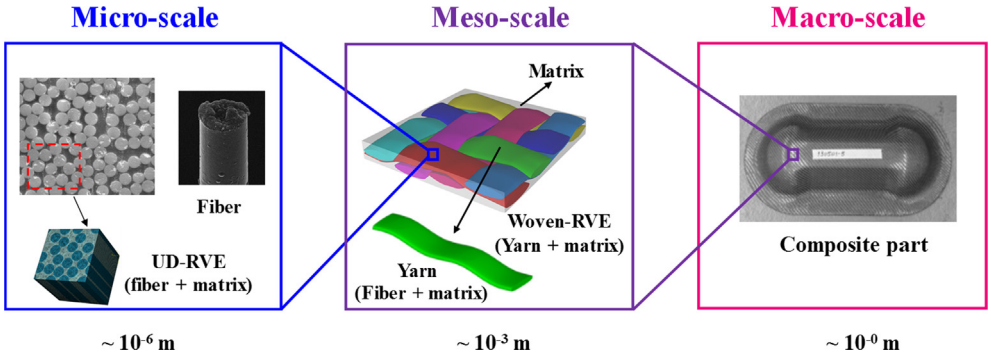

Fig. 1. Illustration of three different scales for woven fabric composites. (For interpretation of the references to colour in this figure legend, the reader is referred to the web version of this article.)

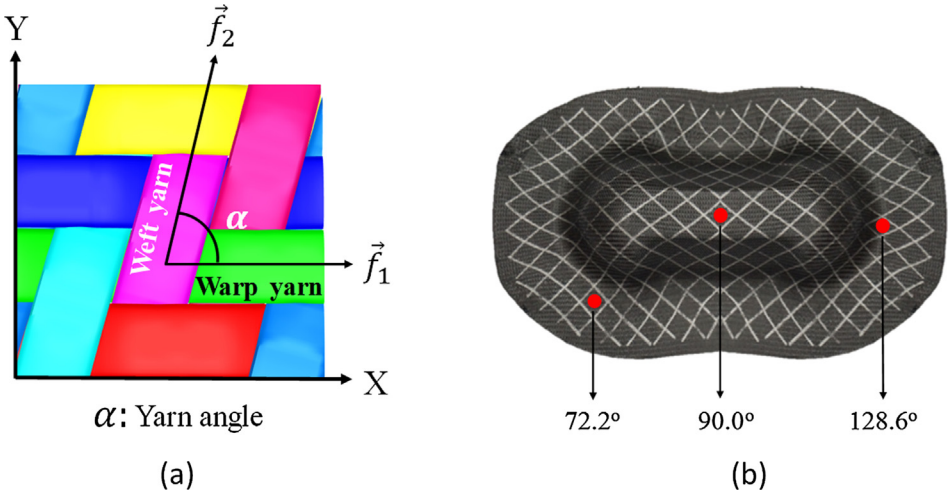

Fig. 2. (a) Yarn angle definition for 2D woven textile composites (resin is hidden); (b) Yarn angle distribution of woven prepreg after preforming (white marker lines represent yarn directions. They were drawn on the un-deformed prepreg and tracked yarn direction during deformation). (For interpretation of the references to colour in this figure legend, the reader is referred to the web version of this article.)

that the material of the cured woven composite part was homogeneous material. This assumption, however, is incorrect when considering the influence of the preforming process, which can result in the material of the woven composite part behaving as a heterogenous material.

In preforming, woven prepregs or fabrics primarily experience in-plane shearing deformation [9–11] to conform the desired 3D geometry from its original flat shape, leading to the yarn angle varying from 90° (the original angle). Fig. 2(b) presents the yarn angle distribution of a double-dome woven prepreg after preforming, in which white curves indicate the yarn directions. Large yarn angle variations from 90° can be observed, particularly in the region that features a double-curvature surface. This yarn angle variation (or yarn angle distribution) would ultimately be inherited by the final cured woven composite part after the curing process. Therefore, to have a high-fidelity performance simulation of the cured woven composite part, it is necessary to investigate the influence of yarn angle variation on the material properties.

On the aspect of experimentally characterizing yarn angle in the deformation, Lomov et al. [12] proposed to use the Digital Image Correlation (DIC) method to obtain the full-field yarn angle distribution within the specimen of 2D textile reinforcements. Kontsos et al. [13] employed the DIC to measure the in-plane strain distribution of 3D woven composites with Z binders.

Several analytic models exist that attempt to predict the material properties of cured woven composites, such as the fiber undulation model and the bridging model [14,15]. These models are based on the classical laminate theory and are only applicable to orthogonal woven composites. For non-orthogonal woven composites, Mitchell et al. [16–18] proposed a finite element model called the double-orthotropic shell model to predict macro-material properties. It was composed of two superposed shells occupying the same spatial space, and each shell was used to model the mechanical contributions of warp or weft yarns. They assumed deformations along the two yarn directions were independent, and there was no tension-shear coupling. However, these assumptions are not appropriate for the actual non-orthogonal woven composites due to the existence of tension-shear coupling [19,20]. Their work demonstrates the necessity to account for the influence of the manufacturing process on the resulting material properties.

Commercial programs such as CATIA and FiberSIM provide the interface for the integrated preforming-performance simulation for the woven composites [14,21]. These interface programs use a fishnet algorithm to predict how the fabric or prepreg would deform into the mold shape. When the deformation shape of the fabric is predicted by the interface, yarn orientations are fed into the associated finite element package. The fishnet algorithm does not consider the mechanical behavior of the material and is purely based on the kinematics. Thus, it is unable to give an accurate prediction for the forming process, particularly when the mold shape is complex and has double-curvature features. Additionally, these interface programs use the classic laminate theory to compute the material properties of cured woven composites. Consequently, the accuracy of these available commercial interface programs is greatly compromised.

To address these issues, in this paper a multi-scale modeling approach is employed to compute the material properties of cured woven composites. Additionally, tension-shearing coupling is considered in the modeling. This paper aims to link the preforming process to the resulting mechanical properties of cured woven composites and build an integrated preforming-performance model for the woven composite part. The outline of this paper is as follows: In Section 2, the detailed multi-scale modeling for computing the material properties of cured

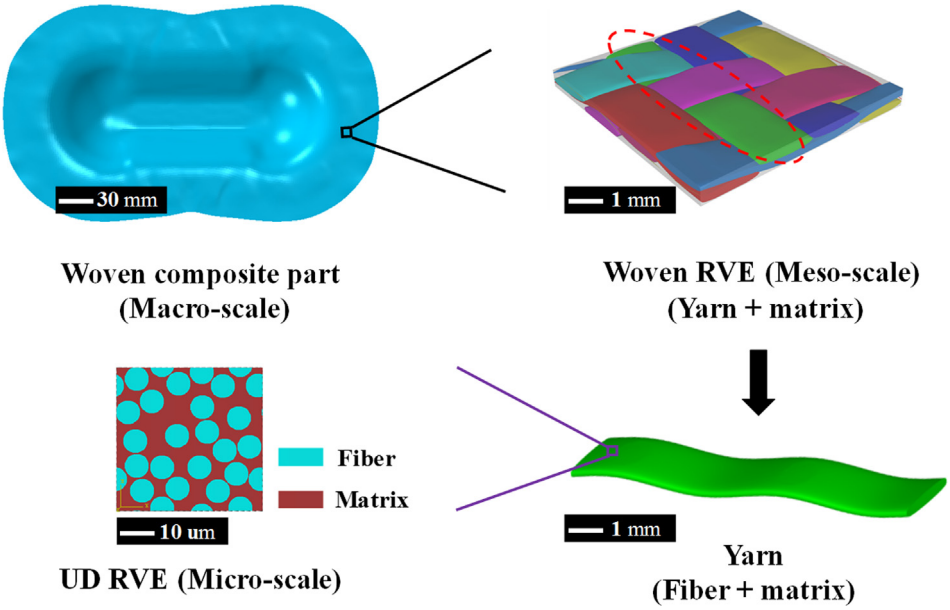

Fig. 3. The multi-scale modeling approach for a woven composite part. (For interpretation of the references to colour in this figure legend, the reader is referred to the web version of this article.)

woven composites with different yarn angles is given. In Section 3, experimental validations of these predicted material properties are presented. In Section 4, an integrated preforming-performance simulation model is proposed for the cured woven-composite part, accounting for the influence of yarn angle variation on the local material properties. Simulations are performed and compared with experiments to demonstrate the effectiveness of the integrated model.

2. Multi-scale modeling of cured woven composites accounting for yarn angle variation

2.1. Framework of the multi-scale modeling approach

To predict the macro-response of cured woven composites under different loading states, the multi-scale modeling approach is employed in this paper due to its high flexibility and low cost compared to the traditional experimental methods. Fig. 3 shows the schematic of the multi-scale modeling approach for a cured woven composite part. For each macro-material point, based on its associated parameters (e.g., yarn angle, overall fiber volume fraction, etc.), a corresponding meso-woven RVE structure is generated, composed of yarns and matrix. Yarn material properties come from the homogenization of its unidirectional (UD) RVE structure, where fibers are randomly distributed in the matrix. By conducting the homogenization over the woven RVE structure, macro-material properties can be identified. The multi-scale modeling method can be used for both single and multi-ply composites. For multi-ply composites, material properties of each ply need to be identified independently with the mentioned multi-scale modeling approach.

2.2. Micro-scale UD RVE modeling

At the micro-scale, each impregnated yarn includes numerous individual fibers embedded in the matrix. To obtain the effective material properties of yarns, a micro-scale UD RVE model is constructed from the microscopic image of yarn cross-sections. UD RVE is a structure containing a certain number of straight fibers within a given domain. Fig. 4 presents the UD RVE geometry model with random fiber distribution in the matrix, generated with an in-house code. The core of this in-house code is based on the fiber random distribution algorithm called RAND_uSTRU_GEN proposed by Melro et al. [22] and

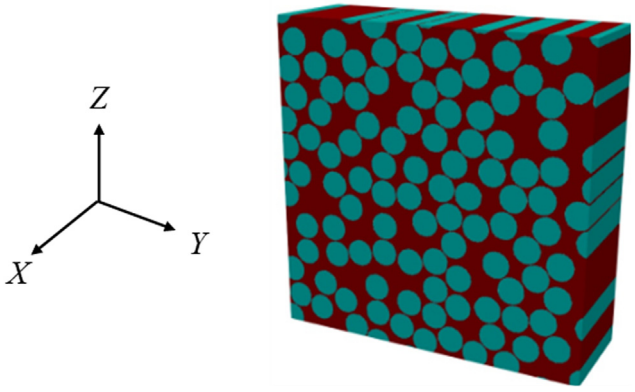

Fig. 4. UD-RVE with randomly distributed fibers in the matrix (fiber volume fraction 0.55). (For interpretation of the references to colour in this figure legend, the reader is referred to the web version of this article.)

implemented in MATLAB. The geometry size of the UD RVE is 42 μm × 42 μm × 8.4 μm and the fibers have a diameter of 7 μm. Voxel meshes were used to discretize the UD RVE structure.

In the micro-scale mechanic analysis, the fiber is modeled as transverse isotropic material, and the epoxy resin is taken as an isotropic material. In this paper, the primary interest is in the elastic deformation range. Thus, it is assumed that the interface between the fiber and the matrix is well bonded and there are no void defects. Table 1 presents the mechanical properties of carbon fiber and epoxy resin taken from the manufacturer's data. The experimental validation of this micro-UD RVE model was already presented in previous work [23,24]. Table 2 presents the homogenization results for a UD RVE with a fiber

Table 1
Fiber and resin properties: the moduli (and G) are all in GPa, X is the fiber longitudinal direction, YZ is the transverse plane perpendicular to the fiber longitudinal direction.

	E_{XX}	$E_{YY} = E_{ZZ}$	$\nu_{XZ} = \nu_{XY}$	ν_{YZ}	$G_{XZ} = G_{XY}$	G_{YZ}
Carbon fiber	245	19.8	0.28	0.32	29.2	5.92
Epoxy resin	3.79	3.79	0.39	0.39	1.36	1.36

Table 2
Predicted yarn mechanical properties with an intra-yarn fiber volume fraction of 0.55 from UD RVE homogenization: the moduli (i.e., E and G) are all in GPa, m-direction is the yarn longitudinal direction, nk is the transverse plane perpendicular to the yarn longitudinal direction.

	E_{mm}	$E_{nn} = E_{kk}$	$\nu_{mn} = \nu_{mk}$	ν_{nk}	$G_{mn} = G_{mk}$	G_{nk}
Yarn	136	9.1	0.32	0.49	4.97	2.79

volume fraction of 0.55, which later would be used as the material properties input into the meso-scale woven RVE homogenization.

2.3. Meso-scale woven RVE modeling

2.3.1. Geometry and mesh generating

Open source software TexGen was used to create the geometry and mesh for the meso-scale woven RVE structure [25]. One key issue is to determine the yarn cross-sectional geometry, yarn path (or yarn center line) and yarn spacing (distance between the two neighbor yarn center lines). The yarn cross-sectional geometry and yarn spacing are impacted by the yarn angle. According to the Micro-CT experimental tests conducted by Barburski et al. [26], for the twill-weave fabric, when the shear angle is less than 30°, its influence on the yarn cross-section and yarn space is small and can be ignored. However, this influence should not be ignored when the shear angle exceeds 30°. Here, it should be highlighted that shear angle and yarn angle are two different concepts, and their relation is as follows: yarn angle(°) = 90° − shear angle(°). Shear angle characterizes the angle change between the two yarn directions as a result of in-plane shear. Therefore, when the yarn angle is confined between 90° and 45°, the corresponding shear angle would range from 0° to 45°, which can cover the possible shear angle value in most shapes of woven textile preforms, such as double-dome and hemisphere. It is true that yarn cross-sectional geometry varies primarily at the yarn cross-overs due to local contact. For the epoxy twill woven composites studied in this paper, small variations of yarn cross-sectional geometry along the yarn path is noted after curing. Thus, the yarn cross-sectional geometry can be assumed to be constant along the yarn path. The geometry parameters of the yarn cross-section, yarn spacing, and yarn path were measured by the optical analysis of microscopic images taken at different locations of cured specimens (Fig. 5(a)). The yarn path was fitted with a smooth B-spline curve, and the yarn cross-section shape was modeled as an elliptical shape. Table 3 summaries the average geometry parameters related to the cured meso-woven RVEs measured from the specimens subjected to the same curing pressure.

Table 3
Geometry parameters characterizing the meso-twill woven RVE structure (mm).

Yarn angle	Yarn width W_y	Yarn height T_y	Yarn spacing S	RVE thickness H
90°	2.46	0.25	2.50	0.58
70°	2.42	0.25	2.45	0.59
60°	2.36	0.26	2.38	0.60
50°	2.23	0.27	2.24	0.62
45°	2.16	0.29	2.16	0.63

In the cured meso-woven RVE geometry structure, the space between yarns is filled with the matrix. Therefore, voxel meshes were used to discretize the yarn and matrix. The meshing was implemented in TexGen (see [4,27] for more details about the meshing strategies). While the quality of the voxel representation of the woven RVE structure improves with refinement, the consequence is that the computation cost would increase. Hence, a balance needs to be found. In Fig. 5(b), the total number of voxel elements (i.e., 8 nodes solid element) in the woven RVE structure (9.8 mm × 9.8 mm × 0.6 mm) is 1,800,000. An accurate representation of yarn geometry can be seen in Fig. 5.

2.3.2. Stress-strain relation for the effective mechanical properties of cured meso-woven RVE

The thickness of the meso-woven RVE structure is orders less than its in-plane dimensions. Thus, it can be assumed under the plane-stress state. The stress-strain relation for the effective elastic properties of a meso-woven RVE structure (including orthogonal and non-orthogonal cases) in the local orthogonal frame 1–2 (shown in Fig. 6) can be written as follows:

$$\begin{bmatrix}\sigma_{11}\\ \sigma_{22}\\ \sigma_{12}\end{bmatrix} = \begin{bmatrix}C_{11} & C_{12} & C_{13}\\ & C_{22} & C_{23}\\ & Symmetry & C_{33}\end{bmatrix}\begin{bmatrix}\varepsilon_{11}\\ \varepsilon_{22}\\ 2\varepsilon_{12}\end{bmatrix} = [\mathbf{C}]_{1-2}[\varepsilon]_{1-2} \quad (1)$$

where $[\mathbf{C}]_{1-2}$ and $[\varepsilon]_{1-2}$ denote the stiffness and strain components in the local orthogonal frame 1–2, respectively. Local axis 1 is coincident with the warp yarn direction. When the yarn angle is not 90°, stiffness

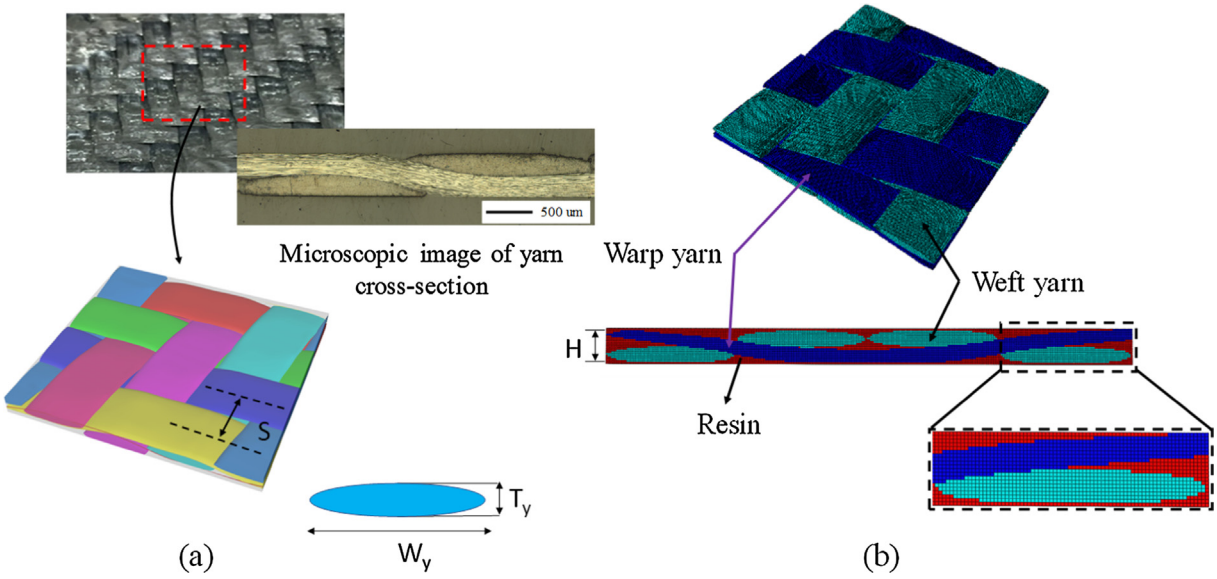

Fig. 5. Meso-RVE of cured woven composites: (a) Geometry model; (b) Discretization with voxel meshes in TexGen. (For interpretation of the references to colour in this figure legend, the reader is referred to the web version of this article.)

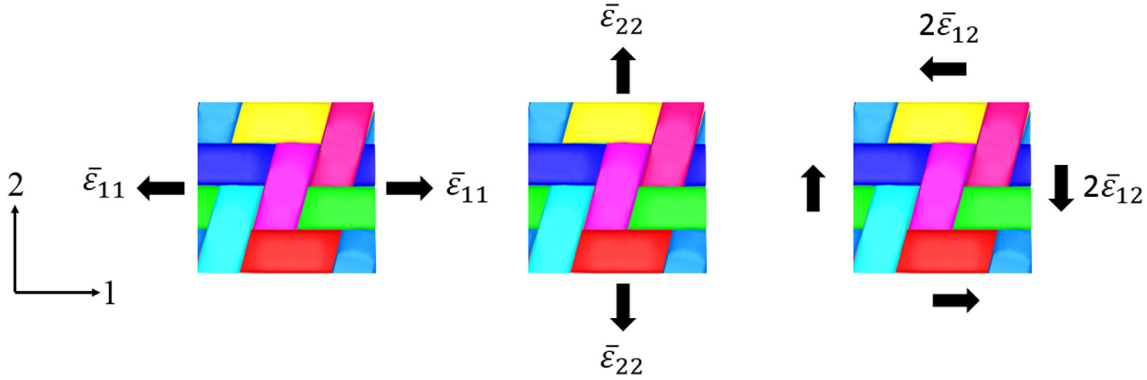

Fig. 6. The three loading states to be solved to calculate the homogenized effective stiffness matrix (for better illustration, the matrix is hidden). (For interpretation of the references to colour in this figure legend, the reader is referred to the web version of this article.)

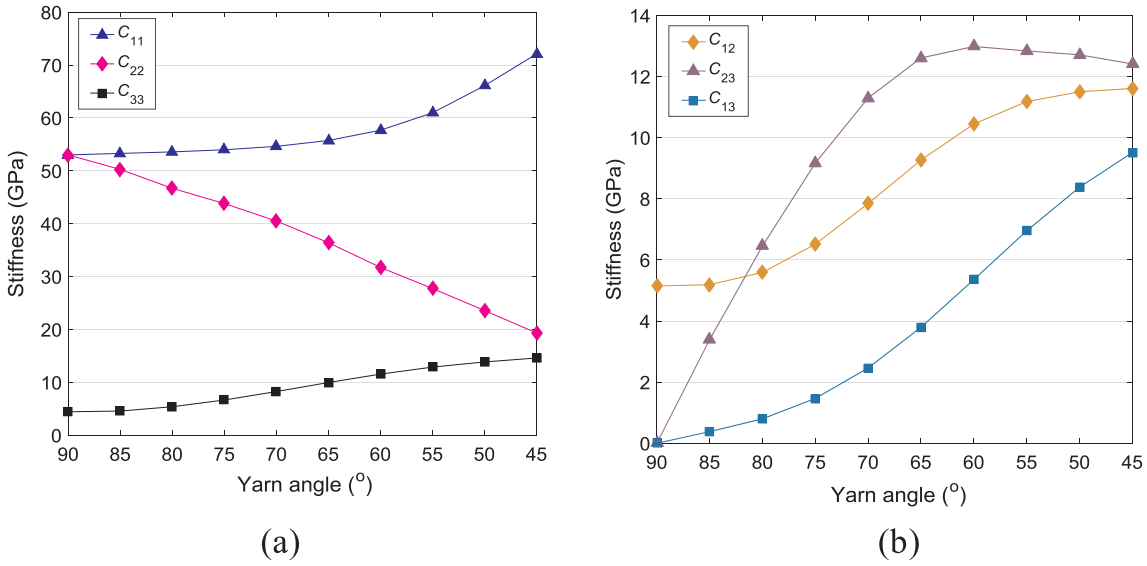

Fig. 7. Woven RVE homogenization results for different yarn angles (intra-yarn fiber volume fraction is 0.55, and the overall fiber volume fraction of the woven RVE is 0.46): (a) Stiffness components C_{11}, C_{22}, C_{33}; (b) Stiffness components C_{12}, C_{13}, C_{23}. (For interpretation of the references to colour in this figure legend, the reader is referred to the web version of this article.)

components C_{13} and C_{23} would be non-zero, characterizing the deformation coupling between the tension and in-plane shear.

Periodic boundary conditions (PBCs) were applied to the RVE at the meso-scale to identify the stiffness matrix $[\mathbf{C}]_{1-2}$. Three loading states were applied individually on the woven RVE boundaries to make it under the uniaxial deformation stress state (in Fig. 6, $\bar{\varepsilon}_{11}$, $\bar{\varepsilon}_{22}$ and $2\bar{\varepsilon}_{12}$ are the applied overall strains). Following the work of Li [28], these applied overall strains need to be transformed into the relative displacements imposed for each pair of nodes on the parallel boundary surfaces in the finite element model. Thus, the relative displacement between each pair of nodes can be written as:

$$u_i^A - u_i^B = \bar{\varepsilon}_{ik}\Delta x_k \tag{2}$$

where Δx_k is the relative distance between each pair of nodes.

The volume averaged stress and strain over the woven RVE structure is then given by:

$$\bar{\varepsilon}_{ij} = \frac{1}{V}\int_V \varepsilon_{ij}dV;\ \bar{\sigma}_{ij} = \frac{1}{V}\int_V \sigma_{ij}dV; \tag{3}$$

where V denotes the volume of the cured woven RVE structure.

Homogenization was implemented in Abaqus/Standard with the above-mentioned periodic boundary conditions. The contact properties between yarns are assumed to be fully contacted, i.e., there is no interfacial sliding and debonding between yarns in the deformation. A post-processing python script was developed to extract and compute the average strain and stress. The averages are then treated as the effective stress and strain in the homogenized woven RVE structure and they are correlated by the effective stiffness matrix$[\mathbf{C}]_{1-2}$. The computation time for each loading state in the homogenization was roughly 8 min when running on HPC (High Performance Computing) clusters with 20 nodes (the total number of the 8-node solid elements of the woven RVE structure was 1,800,000).

RVE size is another important parameter in the micromechanical homogenization analysis. In this paper, RVE size has been examined and increased to two and three times of the RVE size shown in Fig. 6. A small difference is noted for the homogenized properties, which indicates the RVE size in Fig. 6 is large enough and can give convergent homogenized properties.

2.4. Influence of yarn angle variation on the macro-mechanical properties

With the geometry modeling method mentioned previously, a set of cured woven RVE structures with different yarn angles were built, where the yarn angles range from 90° to 45° (RVE geometry parameters are shown in Table 3 in Section 2.3.1). Small variations of the intra-yarn fiber volume fraction is noted with respect to the yarn angle variation (less than 6%) in the actual specimen.

Hence, regardless of the yarn angle change, the intra-yarn fiber

volume fraction of the cured woven RVE structures in the homogenization computation is set as 0.55, which is the averaged value obtained from measurements as discussed in Section 3.1.

Fig. 7 presents the predicted stiffness components versus different yarn angles. It is clearly shown that the stiffness components are significantly impacted by the variation of yarn angle, particularly the stiffness component C_{22}, which almost decreases linearly with the decreasing of the yarn angle. When the yarn angle varies from 90° to 45°, there is about a 60% decrease for C_{22}. The stiffness component C_{11} is along the warp yarn direction (see Fig. 6). As plotted in Fig. 7, it is almost not affected when the yarn angle varies from 90° to 70°; when the yarn angle is smaller than 70°, it starts to have a sharp increase. This increasing is contributed primarily by the stiffness projection of the weft yarns. The tension-shear coupling is denoted by the stiffness components C_{13} and C_{23}. They are zero when the yarn angle is 90° and increase as the yarn angle varies from 90° to 45°, indicating a growing tension-shear coupling for the non-orthogonal woven composites. It is noted that the in-plane shear stiffness component C_{33} also increases with the decreasing of yarn angle; about a 50% difference can be seen when the yarn angle varies from 90° to 45°. These predicted stiffness components later would be used in the performance simulation in Section 4.

3. Experimental validation of the predicted mechanical properties

To validate the predicted stiffness components in Section 2.4, experimental tests were performed for the cured woven samples. One key point is to get samples with non-orthogonal yarn angles, because the cured woven composites provided by the manufacturer generally are orthogonal (yarn angle 90°). To obtain non-orthogonal cured woven samples, special preparation operations are needed.

3.1. Specimen preparation

To generate reliable test data, each test specimen must meet the following requirements: (1) Have a sufficiently large zone with uniform desired yarn angle distribution; (2) Have uniform fiber volume distribution within this zone; and (3) Be well cured with a low content of voids (less than 2%). The geometry of such specimen is sketched in Fig. 8 and Zone B has the desired yarn angle distribution. The average stress-strain relation in the gauge zone (dashed yellow line) is utilized to characterize the mechanical behavior. The specimen was manufactured from the uncured single ply twill-weave prepreg (Carbon-Epoxy) and the detailed preparation procedure is described as follows:

- A rectangular shaped piece was cut from the uncured woven prepreg and a bias-extension test was performed to attain the desired yarn angle distribution in the gauge zone. While the picture frame test can also be applied to shear the woven prepreg, its device is much more complicated than the bias-extension test, and it has a high skill requirement in clamping the sample to the picture frame to ensure the perfect fiber alignment [11,30]. In contrast, the bias-extension test is relatively simple, does not require any special device and can be carried out on any tensile machine. Thus, the bias-extension test is selected for this paper. The bias-extension test was performed at an elevated temperature to make woven prepreg shear more easily than at room temperature. It should be noted that here the purpose of the bias-extension test is just to shear the prepreg to the desired yarn angle, not for measuring its in-plane shear properties. Fig. 9(a) shows a sample that was placed in an oven to allow high temperature bias-extension tests to be conducted. In the bias-extension test, when the initial length of sample (L) is at least more than twice the width of sample (W), there can exist a uniform pure in-plane shearing deformation zone in the center of the sample (region B in Fig. 9(b)) [11,29]. After the bias-extension test, an un-cured woven prepreg with the desired yarn angle distribution in its central zone can be obtained (region B in Fig. 9(c)). To rule out the influence of slippage that may occur in the bias-extension test, the actual value of the yarn angle in the central zone of the sample needs to be measured independently of the clamp-end displacement. Therefore, an optical device is generally used to measure the yarn angle.
- A curing process was then performed for the sheared woven prepreg. During the curing, high temperature and pressure were imposed. The curing device used in the experiment is shown in Fig. 10. The curing pressure was controlled by the motion of the drive rod. An aluminum mold was specifically made for curing the prepreg to ensure the pressure can be uniformly applied (Fig. 10(b)). The suggested curing temperature for the studied woven prepreg is 150 °C. No pressure was applied prior to the specimen reaching 150 °C. Pressure was imposed and increased monotonically to 500 KPa within 1 min and then the load 500 KPa remained constant for 15 mins at 150 °C. After 15 mins in the isothermal phase, the pressure was removed, and the temperature started reducing to room temperature. The thickness of the final cured specimen was 0.60 ± 0.03 mm.

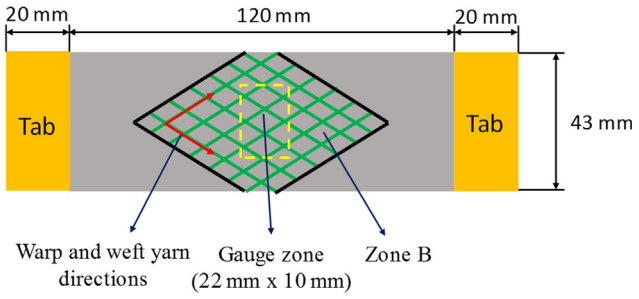

Fig. 8. Geometry of the cured specimen in the experiment. (For interpretation of the references to colour in this figure legend, the reader is referred to the web version of this article.)

Some additional yarn angle changes may be induced by the flow of melt resin under the high pressure of the curing process. Previous studies have found that if the loading path of pressure is imposed appropriately, yarn angle variation caused by the flow of resin can be negligible [30]. This strategy was followed in this paper and noted only small differences for the yarn angle before and after curing (about 3% difference as shown in Fig. 11). The cured specimen was cut into a rectangular shape to remove the squeezed-out resin (Fig. 11) and used in the experimental test. The detailed dimension information of the specimen is shown in Fig. 8.

The intra-yarn fiber volume fraction and the overall fiber volume fraction are important parameters for the proposed multi-scale homogenization model. Therefore, they should be accurately determined. With the assistance of image processing software ImageJ, the intra-yarn fiber volume fraction can be calculated by analyzing the area ratio of fibers in the microscopic image of the yarn cross-section. Several microscopic images were taken at different locations in the gauge zone (Fig. 12). The average value of the fiber volume fraction measured in these images was used to characterize the intra-yarn fiber volume fraction, which was 0.55 ± 0.03. The overall fiber volume in the gauge zone was computed with the density information of the fiber and matrix following the ASTM standard method D792-91 [31]. The measured overall fiber volume fraction in the gauge zone was 0.46 ± 0.02 for all the tested specimens.

3.2. Experimental test

Bias-extension tests were conducted for the cured specimen on a hydraulic testing machine with a load cell capacity of 100 KN. Fig. 13(a) presents the schematic of the bias-extension test and specimen dimensions, and Fig. 13(b) shows the configuration setup. The loading direction was in the center-line of the two yarn directions (y

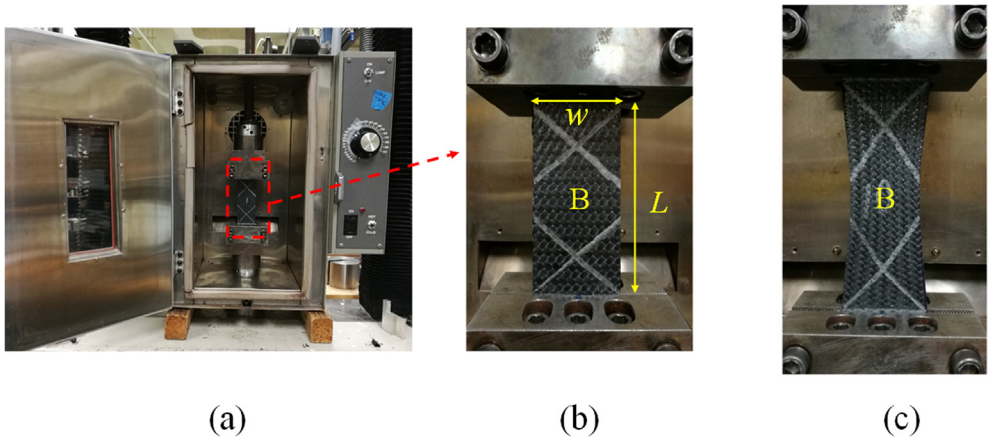

Fig. 9. (a) Bias-extension test for an un-cured woven prepreg in an oven; (b) Un-deformed prepreg (white marker lines follow two yarn directions); (c) Prepreg after bias-extension. (For interpretation of the references to colour in this figure legend, the reader is referred to the web version of this article.)

direction). All tests were quasi-static and limited only in the elastic deformation range. The VIC-3D digital image correlation system (DIC) was used to perform the surface strain measurement of the specimen and the resolution of the CCD camera is 2048 × 2048 pixels. Prior to the testing, surfaces of all the specimens were cleaned with a mixture of water and alcohol to remove the possible pollutions. White background was firstly painted on the one surface of the cured specimen using the spray paint, and later small black spray paint droplets were randomly applied to form high contrast speckle pattern (Fig. 13(b)). During the tests, images of speckle pattern were recorded at a frequency of 2 Hz, and the view field is the whole region of the specimen except for the tab regions.

Each test yarn angle was repeated with three specimens, and their averages were taken as the result of each test yarn angle. Examples are presented in Fig. 14. These curves describe the scatter of the measured stress-strain relations (i.e., the elastic modulus in y direction) in the gauge zone when subjected to the bias-extension. The maximum scatter difference of the elastic moduli to its average is about 3% for the yarn angle 90° and 5% for the yarn angle 75°. The main source of the scatter can be attributed to the yarn angle variation between the specimens that were supposed to have the same yarn angle and equal the target value, which is induced in the sample preparation due to the current manufacturing constraints. Overall, as shown in Fig. 14, the repeatability of the experimental tests is favorable.

3.3. Comparison between the experiment and prediction for the material properties

To facilitate the comparison between the experiment and multi-scale FEA (Finite Element Analysis) prediction, transformations need to be done for the predicted stiffness components in Section 2.3, from the local orthogonal frame 1–2 to the orthogonal reference frame x-y defined in the experiment. The angle θ is measured counterclockwise positive from the x axis to 1 axis as shown in Fig. 15. The following transformation relations exist for the stiffness components [32]:

$$\begin{bmatrix} C_{11}^* & C_{12}^* & 2C_{13}^* \\ C_{12}^* & C_{22}^* & 2C_{23}^* \\ C_{13}^* & C_{23}^* & 2C_{33}^* \end{bmatrix} = [\mathbf{T}]^{-1} \begin{bmatrix} C_{11} & C_{12} & 2C_{13} \\ C_{12} & C_{22} & 2C_{23} \\ C_{13} & C_{23} & 2C_{33} \end{bmatrix} [\mathbf{T}] \tag{4}$$

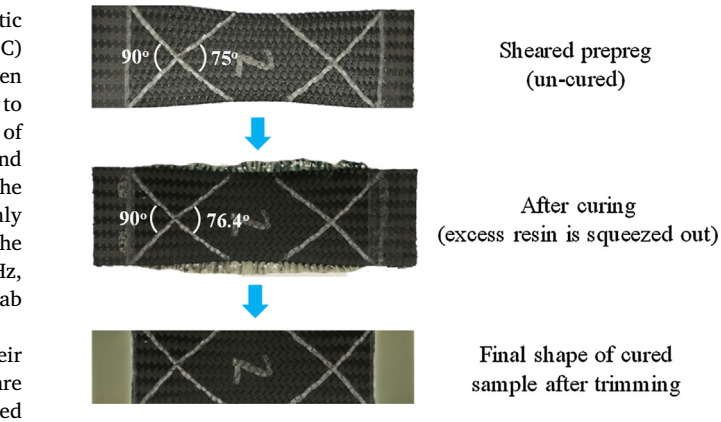

Fig. 11. Preparation process of a cured non-orthogonal woven specimen. (For interpretation of the references to colour in this figure legend, the reader is referred to the web version of this article.)

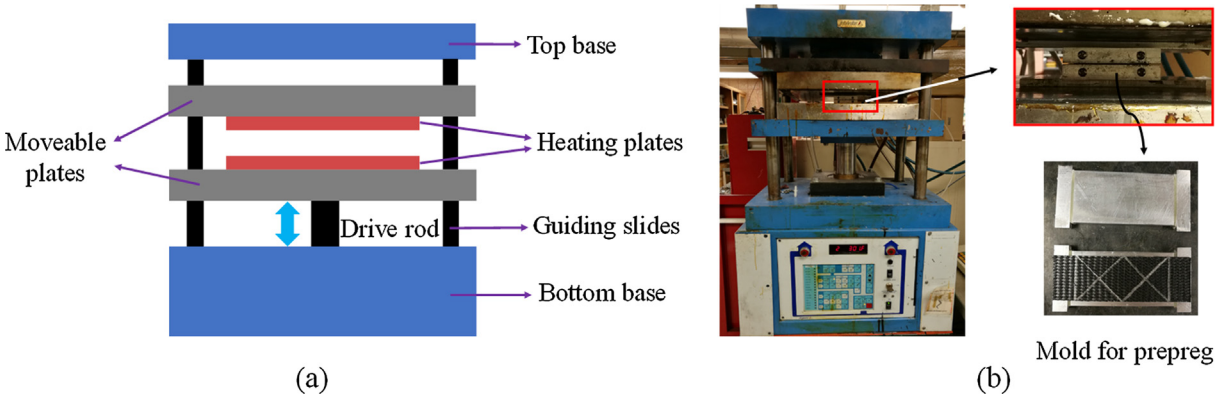

Fig. 10. Curing device for the woven prepreg: (a) Schematics; (b) Actual configuration. (For interpretation of the references to colour in this figure legend, the reader is referred to the web version of this article.)

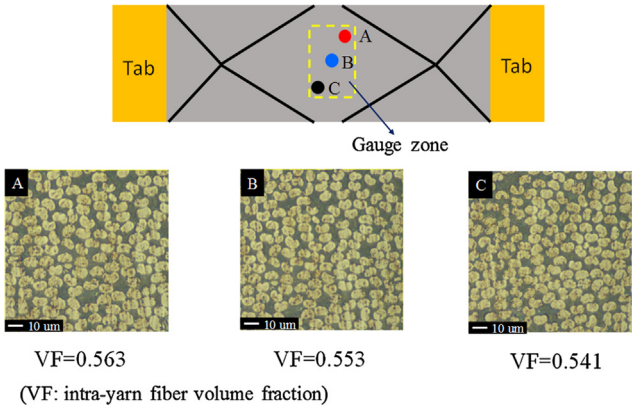

Fig. 12. Local intra-yarn fiber volume fraction measured at different locations in the gauge zone of specimen (light color zones represent fibers). (For interpretation of the references to colour in this figure legend, the reader is referred to the web version of this article.)

where C_{ij}^{*} and C_{ij} denote the stiffness components in the reference frame x-y and local orthogonal frame 1–2, respectively, and [**T**] is the transformation matrix:

$$[\mathbf{T}] = \begin{bmatrix} (\cos\theta)^2 & (\sin\theta)^2 & 2\cos\theta\sin\theta \\ (\sin\theta)^2 & (\cos\theta)^2 & -2\cos\theta\sin\theta \\ -\cos\theta\sin\theta & \cos\theta\sin\theta & (\cos\theta)^2-(\sin\theta)^2 \end{bmatrix} \tag{5}$$

Then the compliance matrix in the reference frame x-y is computed:

$$[\mathbf{S}]_{x-y} = \begin{bmatrix} S_{11} & S_{12} & S_{13} \\ & S_{22} & S_{23} \\ & Symmetry & S_{33} \end{bmatrix} = [\mathbf{C}]_{x-y}^{-1} = \begin{bmatrix} C_{11}^{*} & C_{12}^{*} & C_{13}^{*} \\ & C_{22}^{*} & C_{23}^{*} \\ & Symmetry & C_{33}^{*} \end{bmatrix}^{-1} \tag{6}$$

Following Eq. (6), the elastic moduli in the y direction E_{yy} and the Poisson ratio v_{yx} are calculated as:

$E_{yy} = 1/S_{22}$; $v_{yx} = -S_{12}/S_{22}$ (7)

Fig. 16 presents the comparison between the multi-scale FEA prediction and experimental results for E_{yy} and v_{yx} when the imposed strain was 2.2 x10^{-3} for all the specimens with different yarn angles, which are in the elastic deformation state. A non-linear relation can be noted both for E_{yy} and v_{yx} with respect to the yarn angle. Globally, there is a good agreement between the experiment and FEA prediction. Nevertheless, the predicted value for bothE_{yy} and v_{yx} is a little higher than the experimental results. This overprediction can be partly attributed to the discrepancies between the material properties used in the FEA prediction and the physical properties of the tested specimens. In the FEA prediction, it is assumed the material is perfect, and there are no defects. However, for the material of actual specimens, it is almost impossible to be free of defects due to some practical reasons, leading to the material properties degradation compared to the perfect prediction material. It is also noted that with the decreasing of yarn angle (i.e., the increasing of shear angle), there is an increasing trend for the discrepancy between the experiment and FEA prediction. This can be explained by the fact that when decreasing the yarn angle of the fabric, more yarns would come into contact, resulting in the yarn cross-section shape change and the increasing variation of yarn cross-section shape along the yarn path. In this paper, the influence of the yarn angle on the yarn cross-section shape is considered, but it is assumed that the yarn cross-section shape keeps constant along the yarn path, which is one possible factor leading to the increasing discrepancy observed between experiment and prediction for smaller yarn angles.

4. Integrated preforming-performance simulation model

To have a high-fidelity performance simulation of a cured woven composite part, its yarn orientations and mechanical properties need to be accurately defined. As demonstrated in Figs. 7 and 16, mechanical properties of cured woven composites depend on the yarn angle. Thus, the local mechanical property changes caused by the yarn angle variation need to be considered. Yarn orientation and yarn angle distribution of woven composite parts primarily depend on the preforming process. Many preforming simulation models have been developed over the past years [33–36]. In this paper, an integrated preforming-performance simulation model for the woven composite part is proposed (Fig. 17). It contains two steps. The first step is using the already developed non-orthogonal constitutive model [37] to perform the preforming simulation to compute the yarn orientations and yarn angle distribution within the composite part. The second step is the properties mapping process, including yarn orientation, yarn angle and local stiffness matrix. The local stiffness matrix of cured woven composites is computed with the multi-scale homogenization approach mentioned in Section 2. Compared to the traditional experimental methods, the multi-scale computational homogenization approach is less expensive both in time and cost, and it is able to apply the complex coupling deformations which are difficult to implement in the actual experimental tests. In this section, two examples are given to demonstrate the effectiveness of the proposed simulation model.

4.1. Bias-structure performance simulation

The geometry shape of the bias-structure is shown in Fig. 18 and its

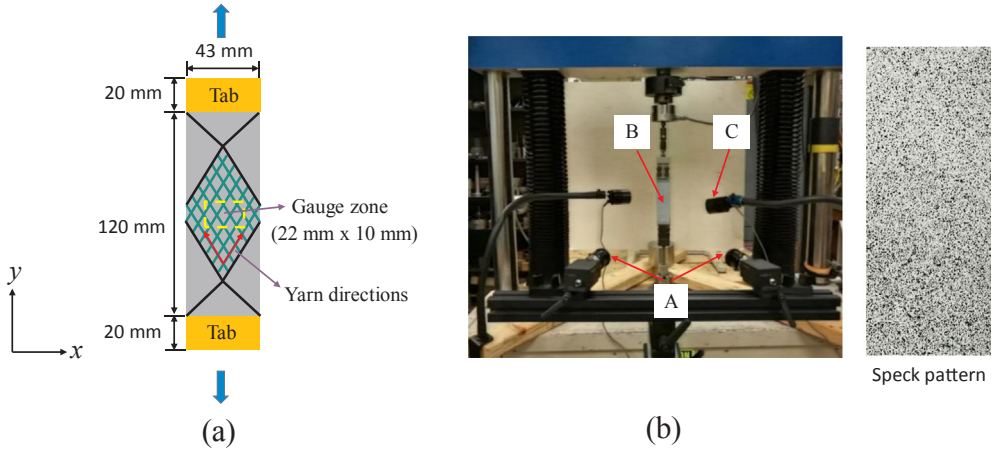

Fig. 13. Bias-extension test: (a) Schematics of the cured woven specimen; (b) Experimental setup: (A) CCD camera; (B) Speckled specimen; (C) Lighting sources. (For interpretation of the references to colour in this figure legend, the reader is referred to the web version of this article.)

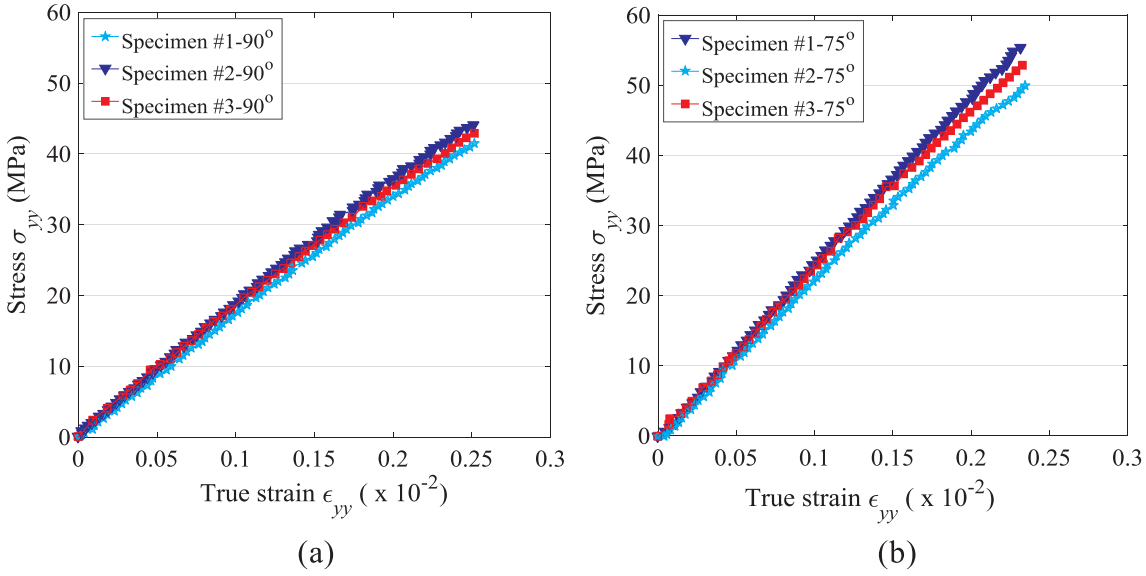

Fig. 14. Repeatability demonstration of the bias-extension tests for the cured woven composites (y is loading direction): (a) Yarn angle 90°; (b) Yarn angle 75°. (For interpretation of the references to colour in this figure legend, the reader is referred to the web version of this article.)

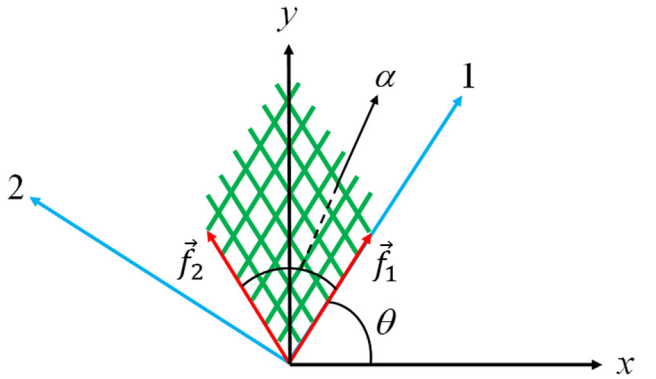

Fig. 15. Transformation between different coordinate frames. (For interpretation of the references to colour in this figure legend, the reader is referred to the web version of this article.)

thickness is 0.6 mm. It is cured and a single ply. Its geometry shape comes from the bias-extension of its uncured prepreg. Preforming simulation was first performed to compute yarn orientations and yarn angle distribution within the bias-structure. As shown in Fig. 18(a), although its shape is simple, large yarn angle variation exists within it. The deformed shape from the preforming simulation was exported and was meshed with the shell elements for the structure stiffness performance simulation. The overall fiber volume fraction was assumed constant within the bias-structure in the simulation. Its value was 0.46, which was measured from the tested specimen. A local orthogonal frame 1–2 was associated with each material point (or integration point). It follows the right-hand rule and the local axis 1 was coincident with the deformed yarn orientation $\vec{f}_1$ (Fig. 18(b)). The in-house developed property mapping packages were utilized to assign the local stiffness matrix in the defined local orthogonal frame 1–2 for each material point based on its yarn angle and overall fiber volume fraction. The user subroutine VUMAT in Abaqus/Explicit was used to update the stress state. The boundary conditions in the simulation and experiment

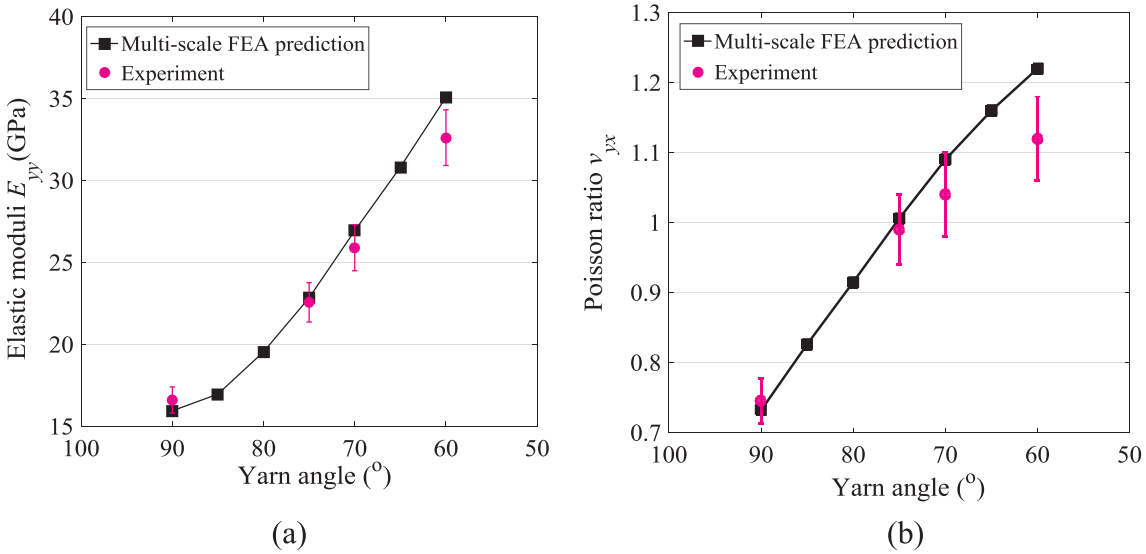

Fig. 16. Comparison between the experiment and FEA prediction for different yarn angles (overall fiber volume fraction is 0.46): (a) Elastic moduli E_{yy}; (b) Poisson ratio ν_{yx}. (For interpretation of the references to colour in this figure legend, the reader is referred to the web version of this article.)

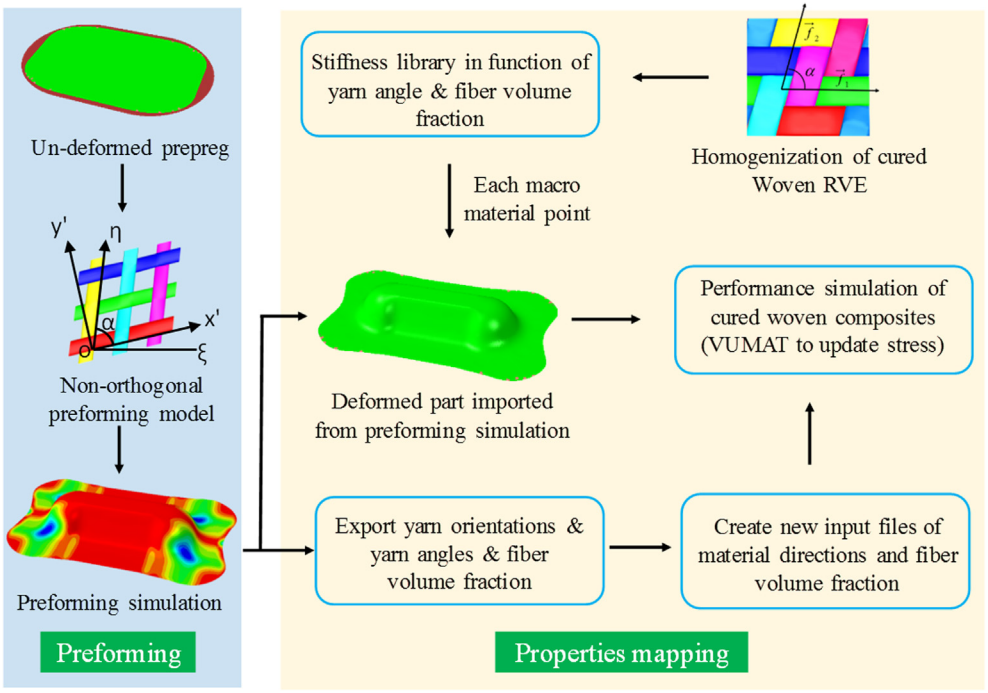

Fig. 17. Flow diagram of the integrated preforming-performance simulation model for the cured woven composite part. (For interpretation of the references to colour in this figure legend, the reader is referred to the web version of this article.)

are presented in Fig. 18(b). One end of the specimen was clamped, and the other end was subject to displacement. In the experiment, digital image correlation (DIC) was used to capture the strain field within the test specimen to compare with the simulation.

Fig. 19 presents the comparison between the simulation and experiment for the strain field within the test specimen when subjected to a displacement of 0.36 mm in the *y* direction (i.e., the equivalent overall strain is 2.92×10^{-3}). It can be seen that the agreement between the simulation and experiment is very good (Fig. 19(a) and (b)). They present very close strain distribution patterns, which agrees well with the distribution pattern of the yarn angle. In the experiment, high local strain concentration can be noted in the intersection region of parts possessing different yarn angles (Fig. 19(b)). It is caused primarily by the sharp change of mechanical properties induced by the yarn angle variation. As shown in Fig. 19(a), this local strain concentration phenomenon is well captured and predicted in the model. Simulations without accounting for the influence of yarn angle variation on the local material properties were also performed, where material properties were assumed constant and equal to the homogenization properties of cured orthogonal woven RVE (yarn angle 90°). All other conditions are the same as those in Fig. 19(a). Fig. 19(c) presents the simulation results. A large discrepancy can be noted between Fig. 19(b) and (c), indicating the inappropriateness of neglecting the influence of yarn angle.

In addition, the force-displacement curve of the bias-structure in Fig. 18 was checked to see the yarn angle variation on the structure's global stiffness. As shown in Fig. 20, simulation accounting for the influence of yarn angle variation on the local material properties gives much better agreement with the experiment for global stiffness (the discrepancy is less than 3%), than the one which does not account for yarn angle variation influence (the discrepancy can reach 20%), which demonstrates the necessity and importance of considering the influence of yarn angle variation in stiffness performance modeling.

4.2. *Double-dome structure preforming-performance simulation*

A double-dome structure has a double curvature surface. Thus, large yarn angle variations can be noted when it is manufactured from woven

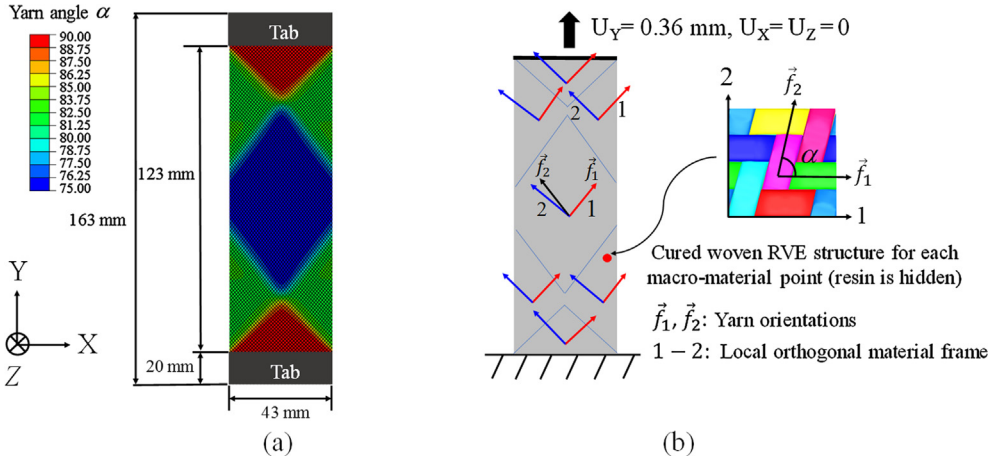

Fig. 18. Bias-structure of cured woven composites: (a) Geometry and yarn angle distribution (from preforming simulation); (b) Boundary conditions and local orthogonal material frame definition in the stiffness performance analysis. (For interpretation of the references to colour in this figure legend, the reader is referred to the web version of this article.)

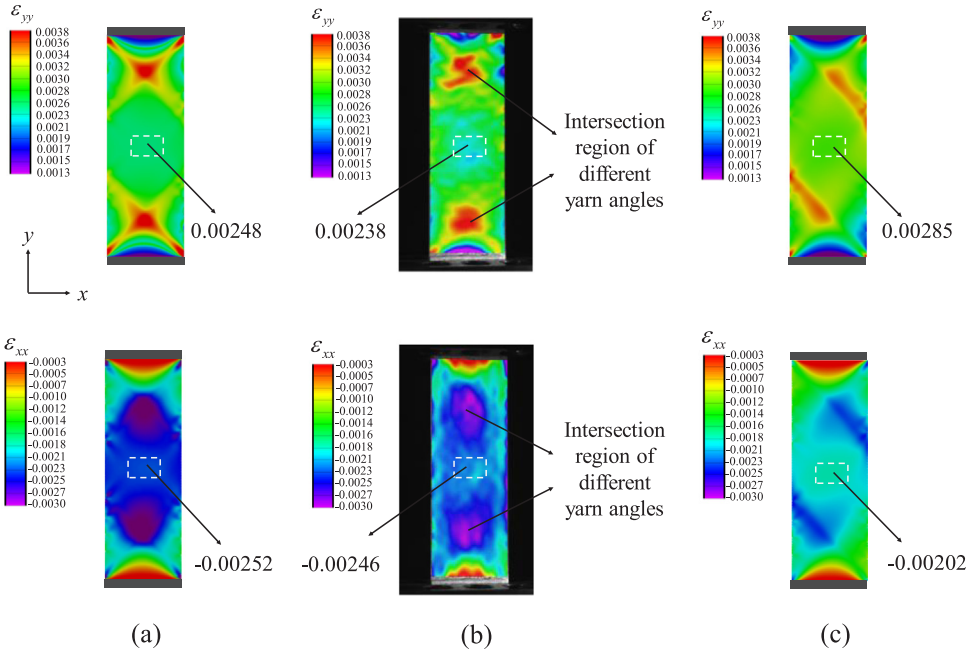

Fig. 19. Strain distribution comparison between simulations and experiments for a cured composite bias-structure when subjected to displacement 0.36 mm in *y* direction (size dimension and yarn angle distribution are shown in Fig. 18(a)): (a) Simulation with yarn angle dependent material properties; (b) Experimental measurement from DIC; (c) Simulation without yarn angle dependent material properties (i.e., the material properties are assumed constant and equal the one where yarn angle is 90°). (For interpretation of the references to colour in this figure legend, the reader is referred to the web version of this article.)

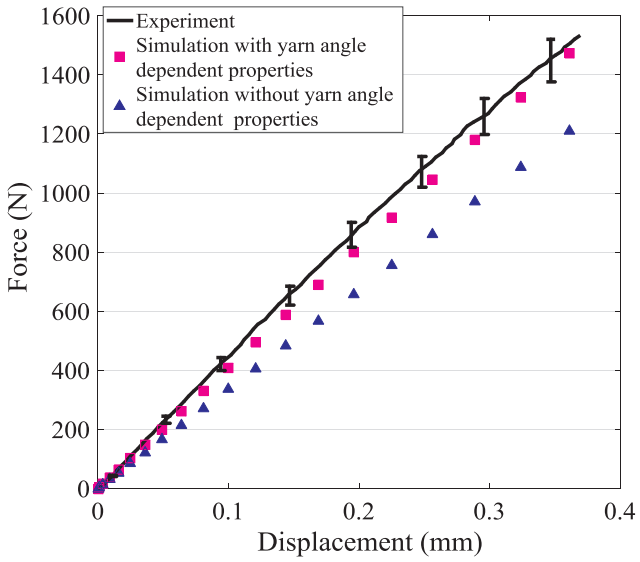

Fig. 20. Force-displacement curve comparison between simulations and experiments for the bias-extension of a cured composite bias-structure (its yarn angle distribution is shown in Fig. 18(a)). (For interpretation of the references to colour in this figure legend, the reader is referred to the web version of this article.)

prepregs in deep stamping. Fig. 21(a) shows the configuration setup for the double-dome preforming simulation. The dimension of the double-dome was the same as the one in the benchmark paper [38]. Two prepreg layers were stacked in the same order, and the initial yarn directions of prepregs were + /−45°. The punch depth was 90 mm. Shell elements (S4R) were used to discretize the prepreg layer. The interfacial behavior between the two neighbor layers was described by the coulomb friction law (according to [39], friction coefficient is 1.2). Fig. 21(b) presents the predicted yarn angle distribution within the double-dome structure after the preforming simulation. The largest yarn angle variation with respect to 90° appears in the region that has the double curvature surface and is about 43°. Yarn angle along a path, which covers the maximum and minimum yarn angles, as shown in Fig. 21(c), was selected for the comparison between the experiment and simulation. As present in Fig. 21(d), the yarn angle predictions are in good agreement with the experiment.

The deformed geometry shape from the preforming simulation was then exported for the structure stiffness performance simulation. The two layers were assumed to be well bonded. Shell elements were used to simulate each layer. The total thickness of the double-dome structure was 1.4 mm and the overall fiber volume fraction was 0.46. These values are the average values measured from the actual double-dome structure. The in-house developed packages mentioned in Section 4.1 were used to assign the local orthogonal material frame and local stiffness for each macro-integration point. The local stiffness matrix is computed with the multi-scale homogenization approach mentioned in Section 2. Fig. 22 shows the boundary conditions, where one end of the double-dome structure was fixed, and the other end was subjected to displacement. Two strain gauges were placed on the tested double-dome structure to measure the strain evolutions and were compared with the simulation (Fig. 22).

Fig. 23 presents the predicted strain distributions when subjected to 1 mm displacement. Strain concentration can be seen in the regions that have large yarn angle variation. Strain comparison between the simulation and experimental values measured from the strain gauges is shown in Fig. 24. A good agreement can be noted both for ε_{XX} and ε_{YY}. The force-displacement curve of the double-dome structure has also been checked. As plotted in Fig. 25, simulation considering the influence of yarn angle variation on the local material properties shows a much better agreement with the experiment, than the one without considering the influence of yarn angle variation. There is about a 10% difference between these two simulations for the predicted global stiffness, which demonstrates the necessity of accounting for the influence of yarn angle on the local material properties.

5. Conclusions

With the multi-scale modeling approach, the mechanical properties of cured woven composites for different yarn angles were predicted and validated by the experiments. To account for the influence of yarn angle variation on the local material properties, an integrated preforming-performance simulation model was proposed for the structure analysis of cured woven composites.

It was identified that yarn angle variation has significant influence on the material properties of cured woven composites and should not be

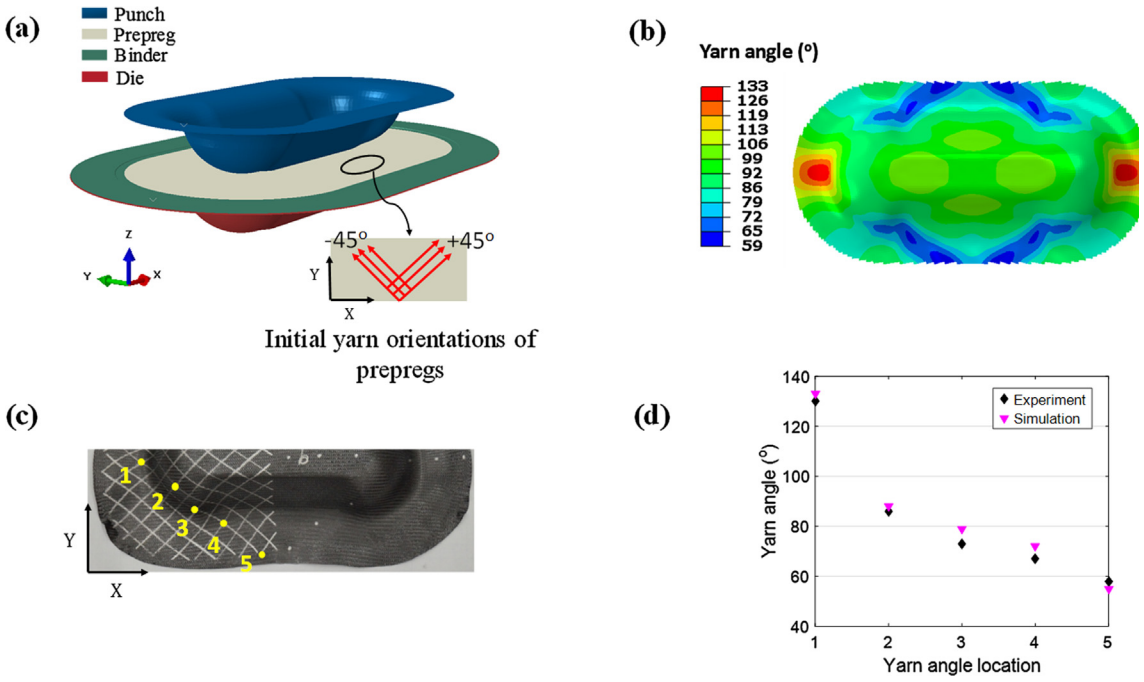

Fig. 21. Double-dome structure preforming: (a) Preforming simulation setup; (b) Predicted yarn angle distribution after preforming; (c) Deformed shape from the experiment; (d) Yarn angle comparison between the simulation and experiment. (For interpretation of the references to colour in this figure legend, the reader is referred to the web version of this article.)

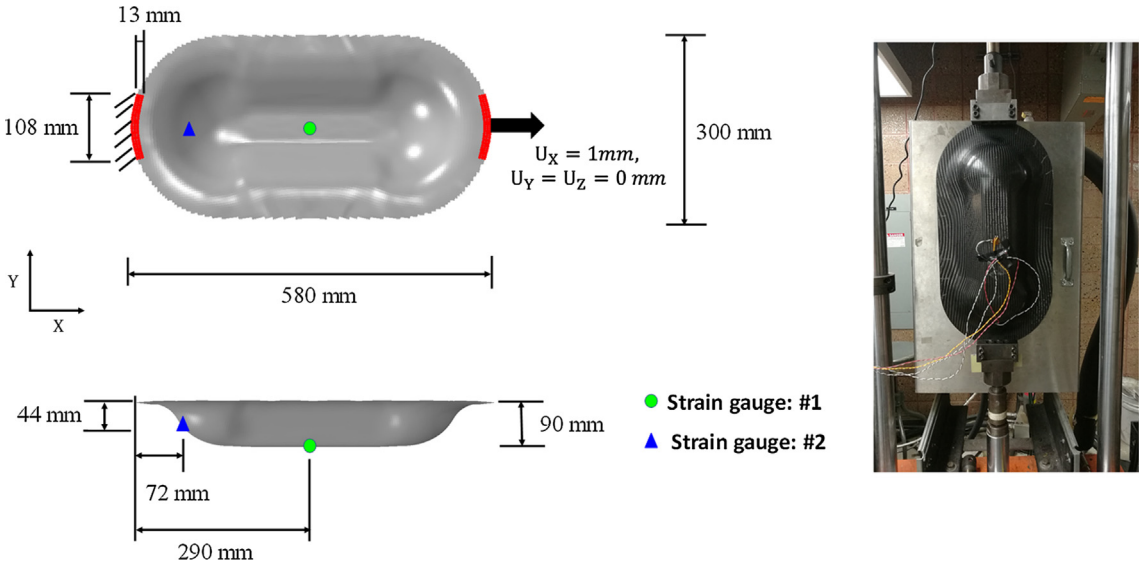

Fig. 22. Boundary conditions and the locations of the strain gauges placed in the test. (For interpretation of the references to colour in this figure legend, the reader is referred to the web version of this article.)

neglected. When the yarn angle varies from 90° to 45°, there is increased tension-shear coupling, and the maximum variation of the tension stiffness component and in-plane shear stiffness component can reach 60% and 50%, respectively (Figs. 7 and 16).

With the integrated preforming-performance simulation model, two simulation cases were performed and compared with the experiments to demonstrate the effectiveness of the integrated model. Non-orthogonal constitutive law was employed in the preforming simulation to compute yarn orientations and yarn angle distribution within the composite part. The in-house developed code was used to assign the local orthogonal material frame and local stiffness for each material point. The results show that the proposed simulation model has more accurate prediction both for the local strain and global stiffness of woven composite parts than the simulation model without accounting for the influence of yarn angle variation (Figs. 19, 20, 24 and 25).

In the currently proposed simulation model, the variations of thickness and overall fiber volume fraction within the composite part were not considered. To further improve the accuracy of the proposed simulation model in the future, their spatial variations should be accounted for. The proposed simulation model demonstrates a very promising method for the structural analysis of woven composites.

Acknowledgement

This work is supported by the US Department of Energy (Award Number: DE-EE0006867).

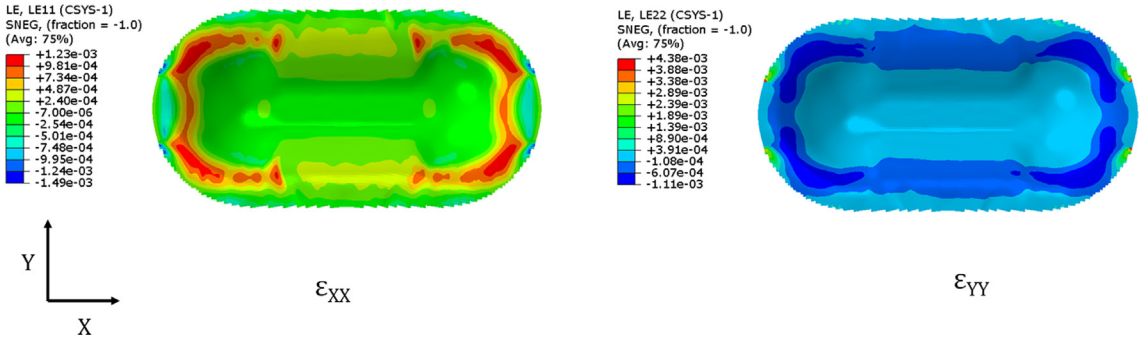

Fig. 23. Strain distribution within the double-dome structure when subjected to 1 mm displacement in the X direction. (For interpretation of the references to colour in this figure legend, the reader is referred to the web version of this article.)

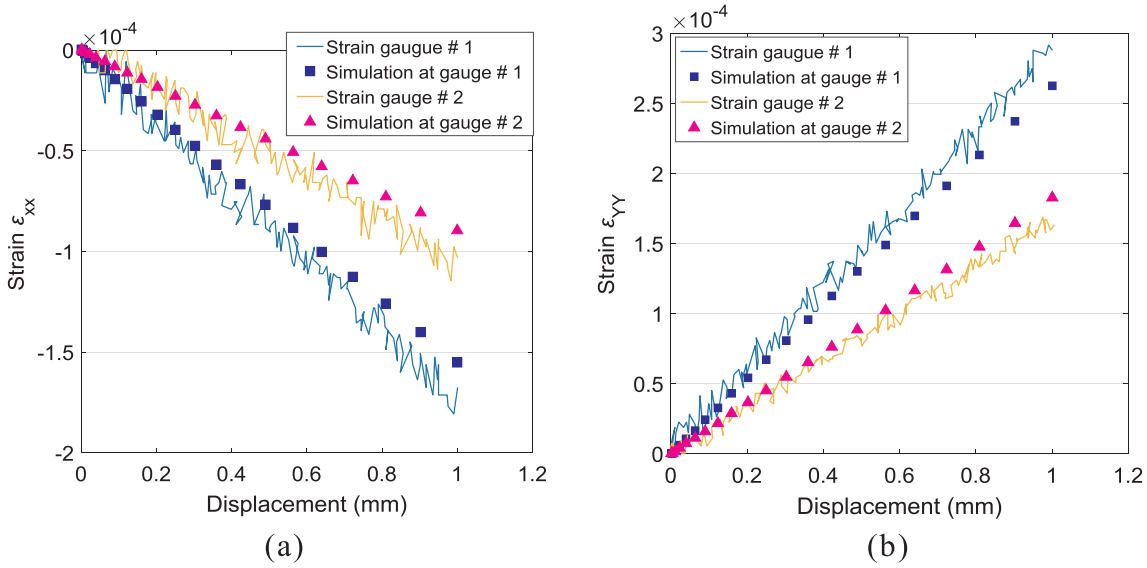

Fig. 24. Strain evolution comparison between the simulation and experiment for double-dome structure: (a) Strain ε_{XX}; (b) Strain ε_{YY}. (For interpretation of the references to colour in this figure legend, the reader is referred to the web version of this article.)

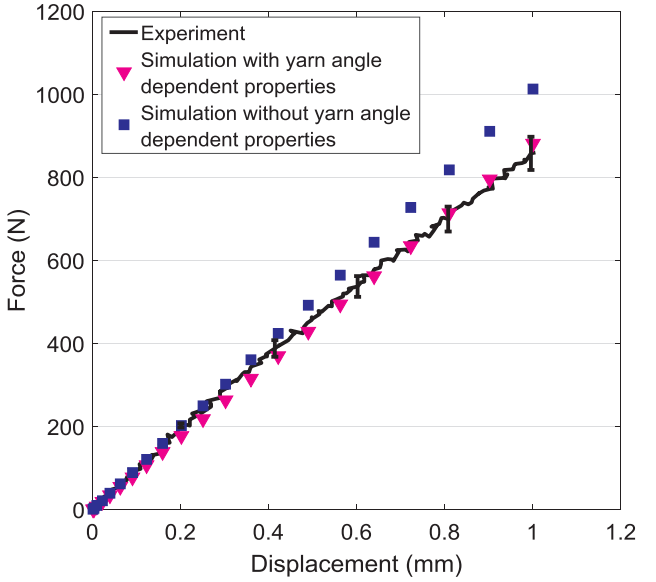

Fig. 25. Force-displacement curve comparison for the double-dome structure between the experiments and two simulations: with and without yarn angle dependent material properties. (For interpretation of the references to colour in this figure legend, the reader is referred to the web version of this article.)

References

[1] Friedrich K, Almajid AA. Manufacturing aspects of advanced polymer composites for automotive applications. Appl Compos Mater 2013;20(2):107–28.
[2] Mangino E, Carruthers J, Pitarresi G. The future use of structural composite materials in the automotive industry. Int J Veh Des 2007;44(3–4):211–32.
[3] Bednarcyk BA, Arnold SM. A multiscale, nonlinear, modeling framework enabling the design and analysis of composite materials and structures. NASA technical report. 2012.
[4] Green S, Matveev M, Long A, Ivanov D, Hallett S. Mechanical modelling of 3D woven composites considering realistic unit cell geometry. Compos Struct 2014;118:284–93.
[5] Huang H, Waas AM. Compressive response of Z-pinned woven glass fiber textile composite laminates: modeling and computations. Compos Sci Technol 2009;69(14):2338–44.
[6] Liu Q, Lin Y, Zong Z, Sun G, Li Q. Lightweight design of carbon twill weave fabric composite body structure for electric vehicle. Compos Struct 2013;97:231–8.
[7] Ning H, Vaidya U, Janowski GM, Husman G. Design, manufacture and analysis of a thermoplastic composite frame structure for mass transit. Compos Struct 2007;80(1):105–16.
[8] Wang L, Wu J, Chen C, Zheng C, Li B, Joshi SC, et al. Progressive failure analysis of 2D woven composites at the meso-micro scale. Compos Struct 2017;178:395–405.
[9] Peng XQ, Guo ZY, Du TL, Yu WR. A simple anisotropic hyperelastic constitutive model for textile fabrics with application to forming simulation. Compos B Eng 2013;52:275–81.
[10] Boisse P, Hamila N, Vidal-Sallé E, Dumont F. Simulation of wrinkling during textile composite reinforcement forming. Influence of tensile, in-plane shear and bending stiffnesses. Compos Sci Technol 2011;71(5):683–92.
[11] Cao J, Akkerman R, Boisse P, Chen J, Cheng H, De Graaf E, et al. Characterization of mechanical behavior of woven fabrics: experimental methods and benchmark results. Compos A Appl Sci Manuf 2008;39(6):1037–53.
[12] Lomov SV, Boisse P, Deluycker E, Morestin F, Vanclooster K, Vandepitte D, et al. Full-field strain measurements in textile deformability studies. Compos A Appl Sci

Manuf 2008;39(8):1232–44.
[13] Castaneda N, Wisner B, Cuadra J, Amini S, Kontsos A. Investigation of the Z-binder role in progressive damage of 3D woven composites. Compos Part A: Appl Sci Manuf 2017;98:76–89.
[14] Naik NK, Shembekar PS. Elastic behavior of woven fabric composites: I—Lamina analysis. J Compos Mater 1992;26(15):2196–225.
[15] Ishikawa T, Chou TW. Stiffness and strength behaviour of woven fabric composites. J Mater Sci 1982;17(11):3211–20.
[16] Mitchell CJ, Dangora LM, Sherwood JA. An Investigation into a robust finite element model for composite materials. Finite Elem Anal Des 2016;115:1–8.
[17] Mitchell CJ, Dangora LM, Bielmeier C, Sherwood JA. Investigation into the changes in bending stiffness of a textile reinforced composite due to in-plane fabric shear: Part 1 – Experiment. Compos A Appl Sci Manuf 2016;85:94–102.
[18] Mitchell CJ, Dangora LM, Bielmeier C, Sherwood JA. Investigation into the changes in bending stiffness of a textile reinforced composite due to in-plane fabric shear: Part 2 – Numerical analysis. Compos A Appl Sci Manuf 2016;85:94–102.
[19] Kashani MH, Hosseini A, Sassani F, Milani AS. Understanding different types of coupling in mechanical behavior of woven fabric reinforcements: a critical review and analysis. Compos Struct 2017;179:558–67.
[20] Launay J, Hivet G, Duong AV, Boisse P. Experimental analysis of the influence of tensions on in plane shear behaviour of woven composite reinforcements. Compos Sci Technol 2008;68(2):506–15.
[21] Cherouat A, Borouchaki H, Giraud-Moreau L. Mechanical and geometrical approaches applied to composite fabric forming. Int J Mater Form 2010;3(2):1189–204.
[22] Melro AR, Camanho PP, Pinho ST. Generation of random distribution of fibres in long-fibre reinforced composites. Compos Sci Technol 2008;68(9):2092–102.
[23] Bostanabad R, Liang B, Gao J, Liu WK, Cao J, Zeng D, et al. Uncertainty quantification in multiscale simulation of woven fiber composites. Comput Methods Appl Mech Eng 2018;338:506–32.
[24] Gao J, Liang B, Zhang W, Liu Z, Cheng P, Bostanabad R, et al. Multiscale modeling of carbon fiber reinforced polymer (CFRP) for integrated computational materials engineering process. Proceedings of the American Society for Composites—thirty-second technical conference. 2017.
[25] Brown LP, Zeng X, Long A, Jones IA. Recent developments in the realistic geometric modelling of textile structures using. TexGen 2013.
[26] Barburski M, Straumit I, Zhang X, Wevers M, Lomov SV. Micro-CT analysis of internal structure of sheared textile composite reinforcement. Compos A Appl Sci Manuf 2015;73:45–54.
[27] Sherburn M. Geometric and mechanical modelling of textiles [PhD thesis]. University of Nottingham; 2007.
[28] Li S. Boundary conditions for unit cells from periodic microstructures and their implications. Compos Sci Technol 2008;68(9):1962–74.
[29] Boisse P, Hamila N, Guzman-Maldonado E, Madeo A, Hivet G, Dell'Isola F. The bias-extension test for the analysis of in-plane shear properties of textile composite reinforcements and prepregs: a review. Int J Mater Form 2017;10(4):473–92.
[30] Drakonakis VM, Seferis JC, Doumanidis CC. Curing pressure influence of out-of-autoclave processing on structural composites for commercial aviation. Adv Mater Sci Eng 2013.
[31] ASTM. ASTM D792-13: standard test methods for density and specific gravity (relative density) of plastics by displacement. West Conshohocken, PA: ASTM International; 2013.
[32] Daniel IM, Ishai O, Daniel IM, Daniel I. Engineering mechanics of composite materials vol. 3. New York: Oxford University Press; 1994.
[33] Gong YK, Peng XQ, Yuan Y, Guo ZY. An anisotropic hyperelastic constitutive model for thermoplastic woven composite prepregs. Compos Sci Technol 2016;128:17–24.
[34] Guzman-Maldonado E, Hamila N, Boisse P, Bikard J. Thermomechanical analysis, modelling and simulation of the forming of pre-impregnated thermoplastics composites. Compos Part A: Appl Sci Manuf 2015;78:211–22.
[35] Peng X, Cao J. A continuum mechanics-based non-orthogonal constitutive model for woven composite fabrics. Compos A Appl Sci Manuf 2005;36(6):859–74.
[36] Liang B, Hamila N, Peillon M, Boisse P. Analysis of thermoplastic prepreg bending stiffness during manufacturing and of its influence on wrinkling simulations. Compos A Appl Sci Manuf 2014;67:111–22.
[37] Zhang W, Ren H, Liang B, Zeng D, Su X, Dahl J, et al. A non-orthogonal material model of woven composites in the preforming process. CIRP Ann 2017;66(1):257–60.
[38] Sargent J, Chen J, Sherwood JA, Cao J, Boisse P, Willem A, et al. Benchmark study of finite element models for simulating the thermostamping of woven-fabric reinforced composites. Int J Mater Form 2010;3(1):683–6.
[39] Zhang W, Ma X, Lu J, Wang QJ, Su XM, Zeng D, et al. Characterization and numerical modeling of the interaction between carbon fiber composite prepregs during a preforming process. J Manuf Sci Eng 2018;140(8):081003.